Supporting Information

HgS and HgS/CdS Colloidal Quantum Dots with Infrared Intraband Transitions and Emergence of a Surface Plasmon

Guohua Shen and Philippe Guyot-Sionnest

James Franck Institute, the University of Chicago, 929 E. 57th Street, Chicago IL 60637

List of supporting information

1. Experimental methods
2. High-resolution TEM images of HgS CQDs
3. Interband absorption spectrum of HgS CQDs before and after surface sulfide treatment
4. Intraband absorption and photoluminescence (PL) spectra of HgS CQDs before and after surface sulfide treatment
5. Effects of environmental conditions on the HgS CQDs synthesis
6. TEM images of HgS CQDs obtained with different Hg:S precursor ratios
7. TEM images of HgS CQDs obtained with different solvents
8. HgS CQDs with different reaction times
9. β-HgS bandgap calculation
10. HgS CQD doping density calculation
11. Intraband absorption of 14.5 nm HgS fitted with Lorentzian and Gaussian functions
12. Local field effect shift for QD^{2-}
13. CdS nanorods synthesis
14. Interband quantum yield of HgS/CdS core/shell
15. Reference

1. Experimental methods

HgS CQDs surface sulfide treatment

1 mL of HgS/TCE solution which had an interband shoulder absorption around 0.1 O.D./cm was put into a test tube. 1 mL of formamide, 50 μL oleylamine and 150 μL 0.1 M $(NH_4)_2S$ in formamide were added into the test tube, stirred for 8 min and the bottom layer (TCE) was kept. Formamide was used to wash the bottom layer twice to remove the excess $(NH_4)_2S$. The solution was ready for FTIR and other measurements. The addition of oleylamine is necessary to keep the dots in the TCE phase.

Spectroelectrochemistry

The spectroelectrochemistry is done in attenuated total reflectance (ATR) configuration. The advantage of ATR-echem is that the signal is much stronger and cleaner than other configurations such as reflection.

A ZnSe window is used in the experiment. First, the window is cleaned carefully and then we use a sputter-coater to deposit a 4 nm Pt/Pd metal layer on ZnSe surface. This metal layer serves as the working electrode. Then we deposit a film of HgS CQD on top of the metal, as described in the main text. The reference electrode is a silver wire and the counter electrode is Au. The electrolyte used is 0.1M $LiClO_4$ in H_2O.

2. High- resolution TEM images of HgS CQDs

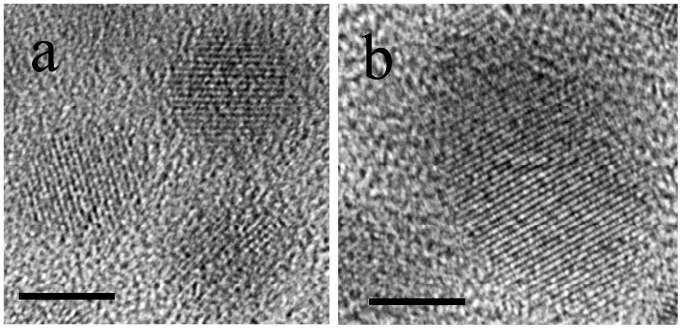

Figure S1. High-resolution image of (a) 6 nm and (b) 14 nm HgS CQDs (scale bar: 5 nm)

3. Interband absorption spectrum of HgS CQDs before and after surface sulfide treatment.

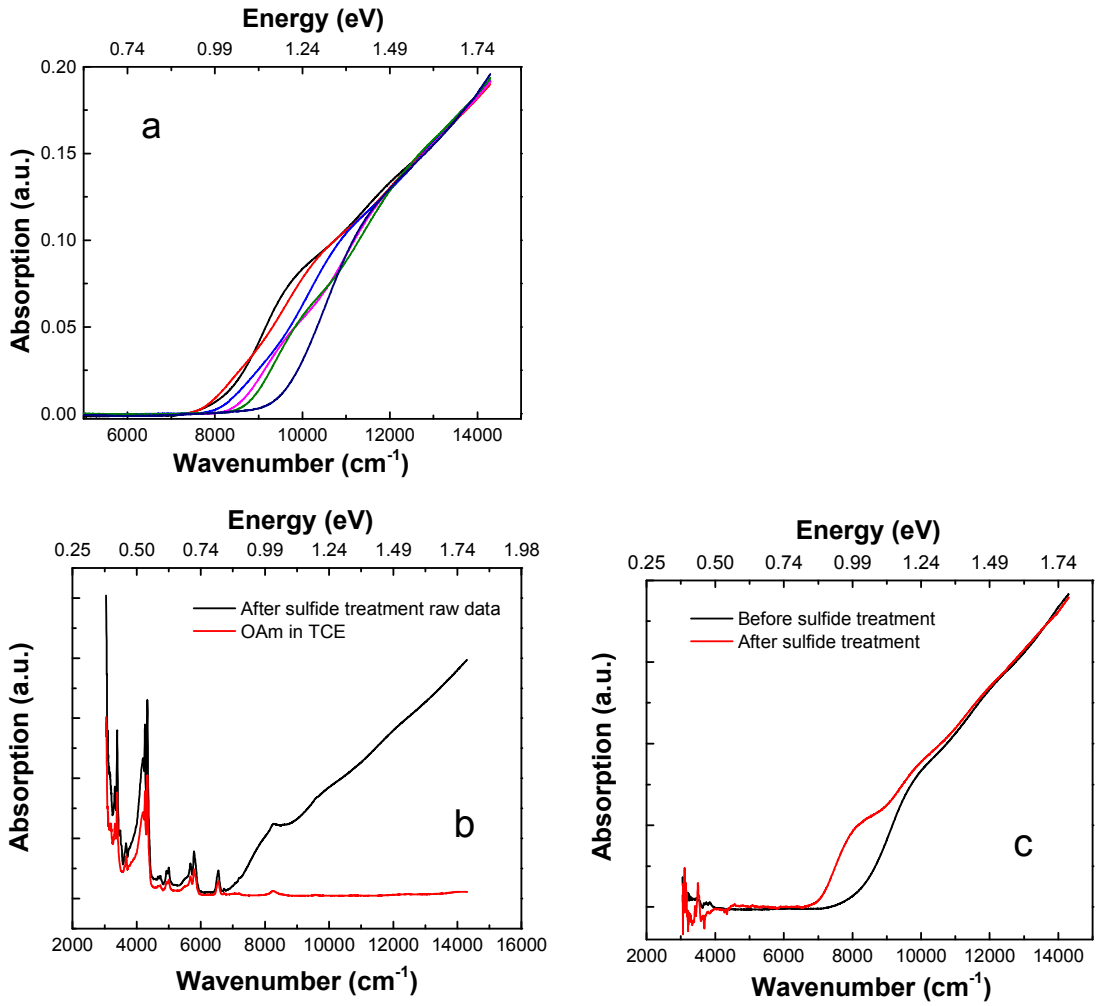

Figure S2. (a) Interband absorption spectra of HgS quantum dots of different sizes before sulfide treatment; (b) Raw data of interband absorption of 5.7 nm HgS quantum dots after sulfide treatment (black) and spectrum of OAm in TCE (red); (c) Interband absorption spectra of 5.7 nm HgS quantum dots before (black) and after sulfide treatment, after substracting the OAm spectrum.

The interband absorption spectra of HgS quantum dots of different sizes before sulfide treatment were shown in Figure S2a. The raw data of the interband absorption spectrum of 5.7 nm HgS quantum dots was shown in Figure S2b. In Figure S2b, the black curve is the spectrum of HgS CQDs after sulfide treatment. There are several small peaks due to the excess oleyamine in the system. In order to get a clean spectrum, the spectrum of

OAm in TCE is subtracted to obtain the spectra in Figure S2c. It is clear that after the sulfide treatment, the HgS shows an exciton at ~7500 cm^{-1} which is not present in the spectrum before sulfide treatment. The sulfide treatment is therefore used to un-dope the HgS CQDs.

4. Intraband absorption and PL spectra of HgS CQDs before and after surface sulfide treatment

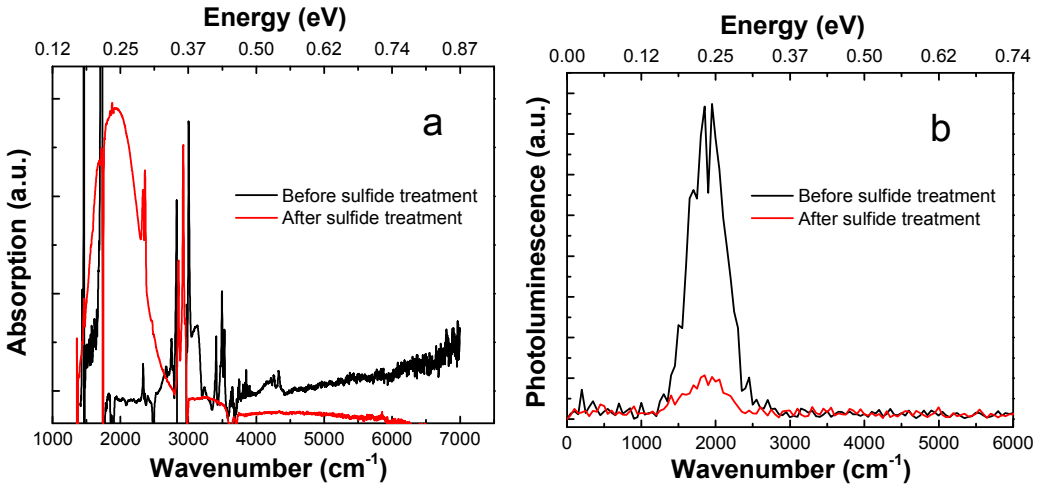

Figure S3. (a) Intraband absorption spectrum of HgS CQDs before and after sulfide treatment; (b) PL spectrum of HgS CQDs before and after sulfide treatment

Figure S3a and S3b show that the intraband absorption and PL almost quenched after sulfide treatment. This also indicates that the $1S_e$ state of the HgS CQDs is fully un-doped after the sulfide treatment.

5. Effects of environmental conditions on HgS CQDs synthesis

Effects of inert atmosphere

Both TEM images and spectra in Figure S4a and S4b confirm that there is no difference whether or not an inert atmosphere is applied.

a

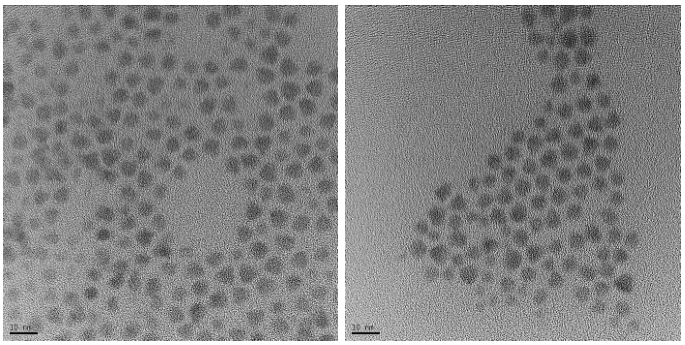

b

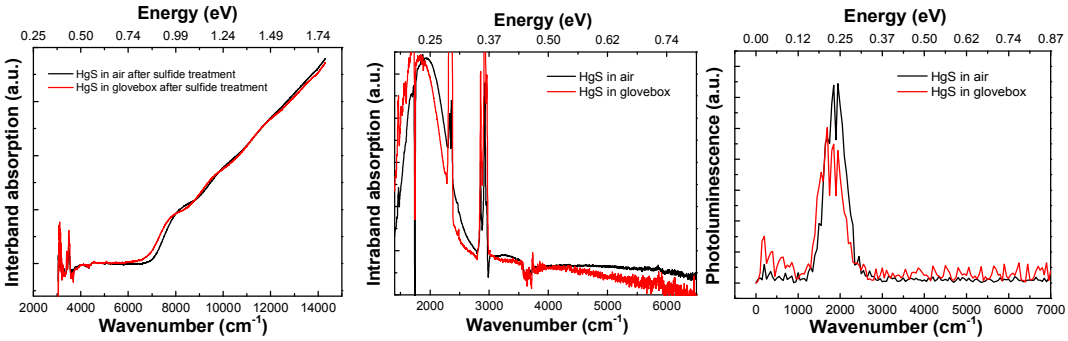

Figure S4. (a) TEM images of HgS synthesized under ambient conditions (Left) and under N_2 (Right); (b) (From left to right) Interband, intraband absorption and PL spectra of HgS synthesized under different conditions

Effects of temperature

Using the same Hg:S ratio (1:30), the same reaction time and solvents (H_2O), but increasing the temperature to 40℃ resulted in a worse size dispersion compared with HgS CQDs obtained under ambient temperature (20℃), shown in Figure S5.

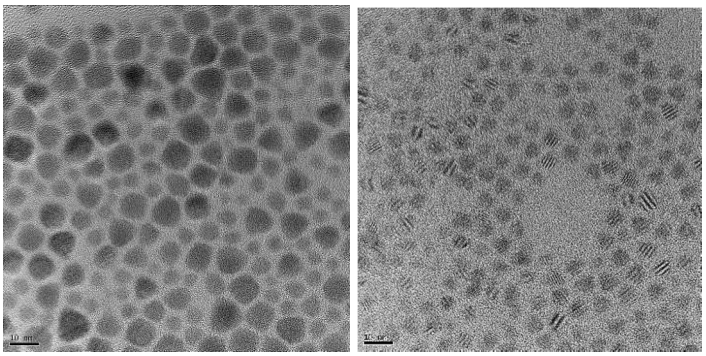

Figure S5. TEM images of HgS CQDs synthesized at 40℃ (Left) and 20℃ (Right)

6. TEM images of HgS CQDs obtained with different Hg:S precursor ratios

Figure S6 shows that the HgS CQDs sizes decrease with increasing Hg:S ratios.

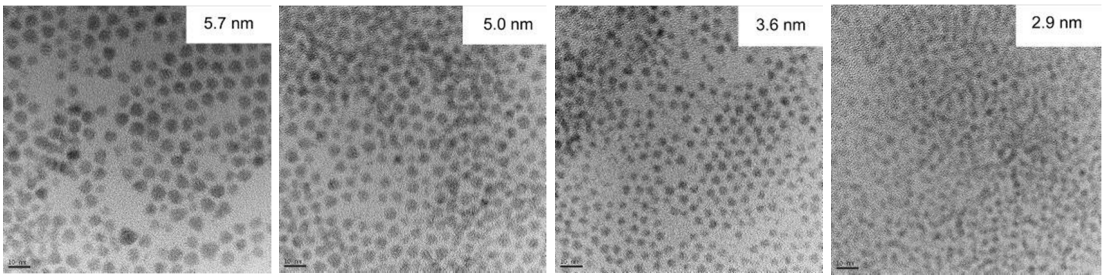

Figure S6. TEM images of HgS CQDs with different Hg:S ratios (from left to right): 1:30; 1:15; 1:5; 1:2

7. TEM images of HgS CQDs obtained with different solvents

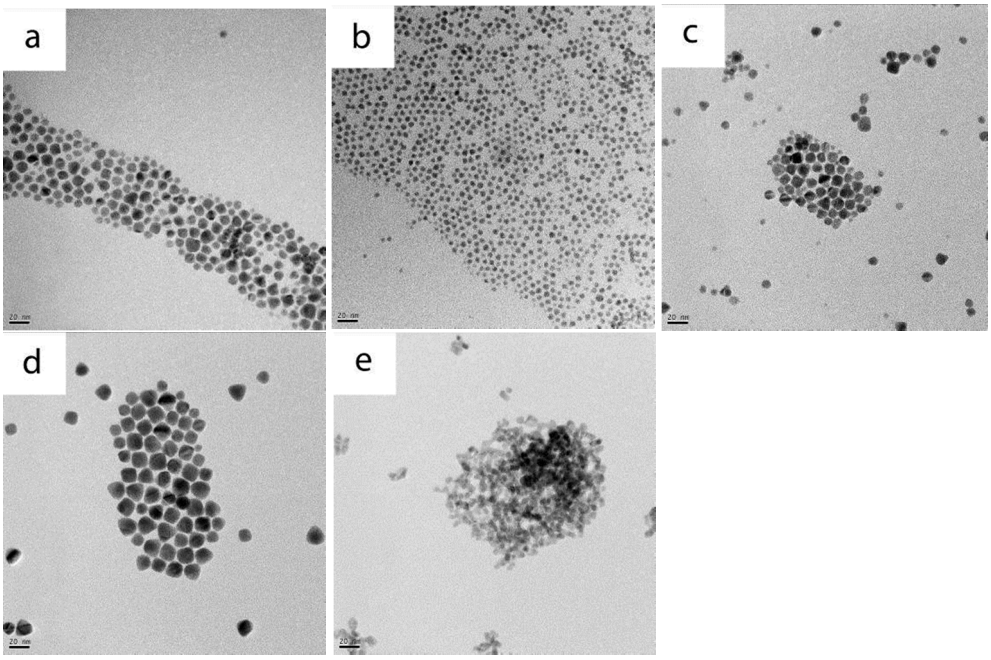

Figure S7. TEM images of HgS CQDs using (a) FA; (b) H_2O; (c) 1:1 FA:ethanol; (d) Propylene carbonate; (e) DMSO as the solvent for $(NH_4)_2S$.

8. HgS CQDs with different reaction time

   The sulfur precursor was 20 μL of $(NH_4)_2S$ dissolved in 2 mL of propylene carbonate and the Hg:S ratio is 1:30.

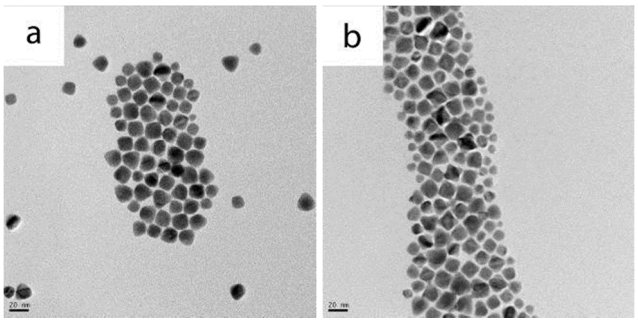

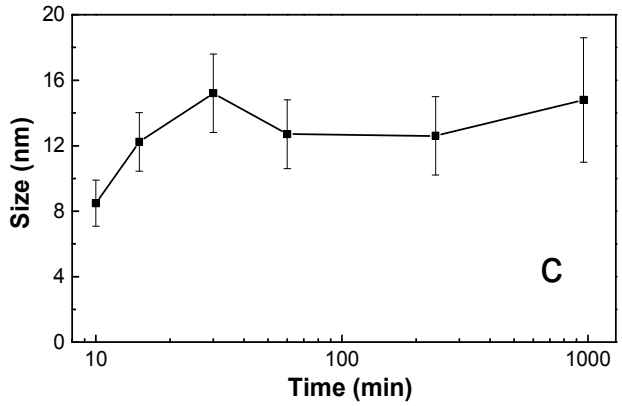

Figure S8. TEM images of HgS CQDs with (a) 30 min; (b) 16 h reaction times; (c) A plot of the CQD sizes with time (*x*-axis is in log scale). The error bars are the standard deviations of the particle size distributions. The data show uniform growth at early times followed by a stable mean size but broadening distribution at longer times.

Figure S8a and S8b presents the TEM images of HgS CQDs after different reaction times. Figure S8c shows that reaction times from 0−30 min steadily increase the particle size with similar monodispersity, consistent with the CQDs being in the growth regime. Reaction times from 1−16 hours begin to show an increased size distribution with no significant growth. This is attributed to the Ostwald ripening regime as the reagents are consumed.

9. *β*-HgS bandgap calculation

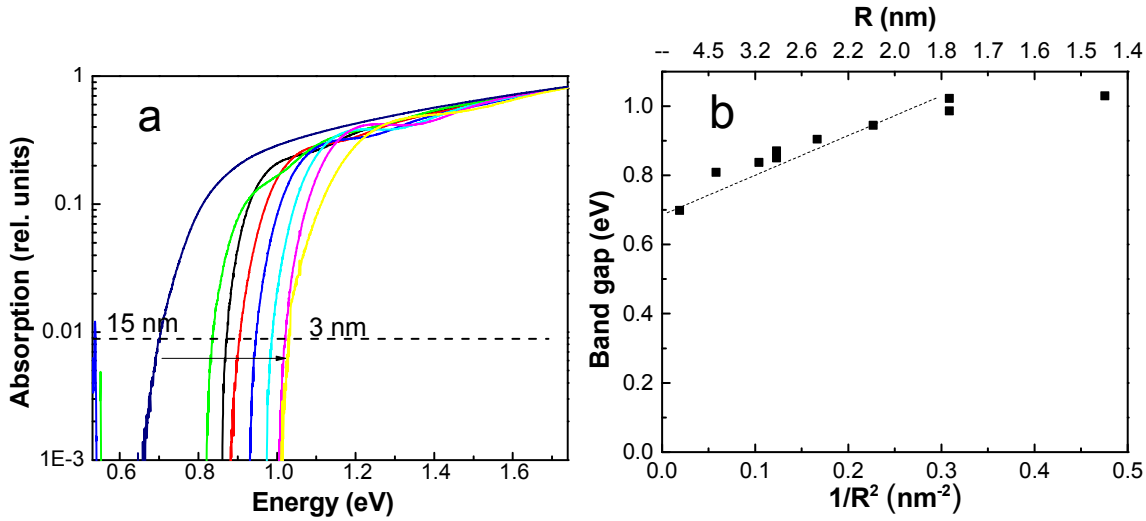

Figure S9. a) Interband absorption of the HgS quantum dot solutions on a log scale. The value of the energy at ~1% of the optical absorption at 14000cm^{-1} is in the sharply decreasing regime consistent with optical absorption by phonons just below the gap. b) β-HgS energy gap versus $1/R^2$. R is the particle radius.

Figure S9a and S9b shows the determination of the bandgap by plotting the interband absorption at about 1% of the absorption at 14000 cm^{-1} versus $1/R^2$. The linear regression has a y-intersect around 0.67 $\pm$ 0.05 eV, which is taken as the β-HgS bandgap. We note that the spectrum of the larger dot, which is doped, has a broader edge evident in Figure S9a, even though its intraband absorption indicate a significant narrowing (Figure 7a). We think that this reflects the fact that plasmonic resonances have intrinsically larger homogeneous broadening than single electronic transitions.

10. HgS CQD doping density calculation

The doping density is calculated from the interband absorption spectra of HgS CQDs before and after the sulfide treatment. Figure S10a and S10b show the results from a 5.7 nm HgS CQD.

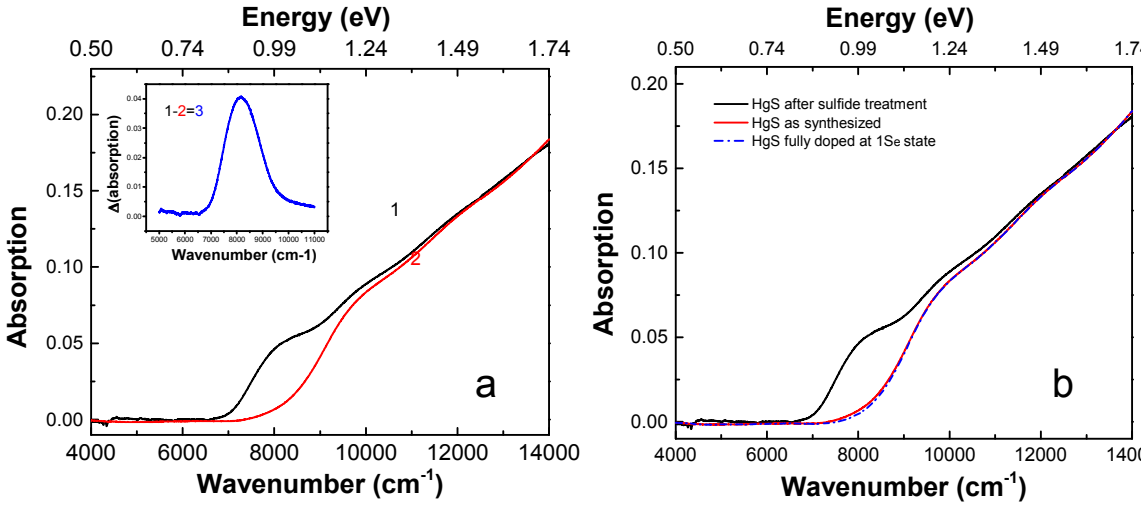

Figure S10. (a) Interband absorption of HgS particles before (red) and after (black) sulfide treatment. Inset: the curve from the subtraction of black and red lines, representing the optical absorption from $1S_e$ state; (b) Derived absorption of HgS fully doped at $1S_e$ state (dashed blue line)

Figure S10a is the same as Figure S2b, where the red line is the absorption of HgS as synthesized and black line after sulfide treatment. The difference of the two curves comes from the result that sulfide treatment un-dopes the $1S_e$ state of the HgS CQD. The subtraction between these two absorption spectra results in the blue curve in the inset (curve3), which accounts for the spectral change due to the change in doping. We note that it shows a single peak as expected if only the $1S_e$ state occupation is modified. The next step is to subtract the blue curve in Figure S10a from the black curve as much as possible to completely bleach the 1S exciton. The result is shown as the dashed blue line in Figure S10b. The relationship is as followed:

$$HgS\ fully\ doped\ curve = curve1 - A * curve3$$

where A is the subtracting parameter. In this case, $A = 1.04$.

The $1S_e$ peak position comes from the Gaussian fitting of the subtraction. The fitting peak is 8237 cm^{-1} in this case. So the final doping density is:

$$\text{Number of } e^- \text{ per dot} = 2 \times \frac{\text{Abs(black, 8237 cm}^{-1}\text{) - Abs(red, 8237 cm}^{-1}\text{)}}{\text{Abs(black, 8237 cm}^{-1}\text{) - Abs(blue, 8237 cm}^{-1}\text{)}}$$

where Abs(black/red/blue) is the absorbance from black/red/blue spectrum in Figure S10b. The calculated result is 1.92 e^-/dot, which is the natural doping density of 5.7 nm HgS CQDs as synthesized.

The error of this method comes from two factors. First, there is the choice of the subtracting parameter A. In our method, A could be determined within 0.1, as shown in Figure S11.

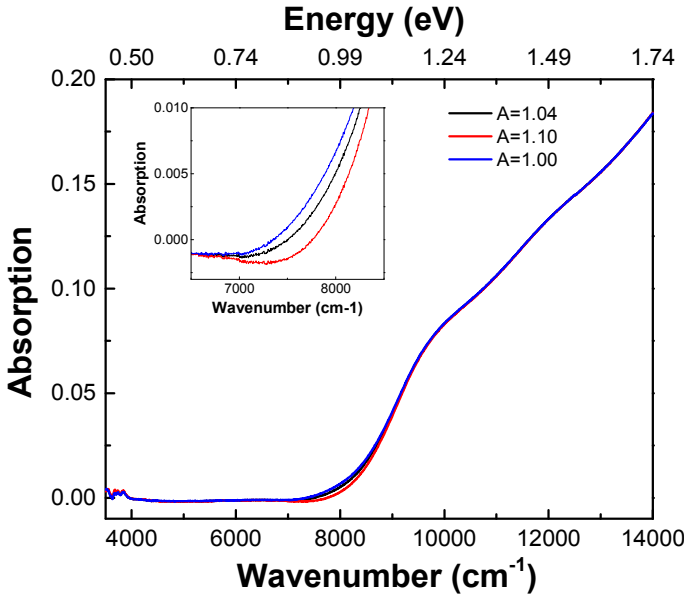

Figure S11. Derived absorption of HgS fully doped at $1S_e$ state with different A values (inset: zoom in of the absorption curves)

The red curve shows an unphysical decrease in absorption around 7500 cm^{-1}, which is a sign of over-subtraction. The blue curve is under-subtraction and could subtract further to get the black curve. The error from different A values is $\pm$ 0.1 e^-/dot.

Another source of error comes from the line width of the Gaussian fitting for curve3. The FWHM of curve3 covers wavelength from 7500 cm^{-1} to 8900 cm^{-1}. And within this range, the deviation of doping density is less than $\pm$ 0.01 e^-/dot. As a result, this error is negligible compared with the error coming from the uncertainly of A.

The combined error is then $\pm$ 0.1 e^-/dot, which also applies to other sizes based on similar calculation process.

11. Intraband absorption of 14.5 nm HgS fitted with Lorentzian and Gaussian functions

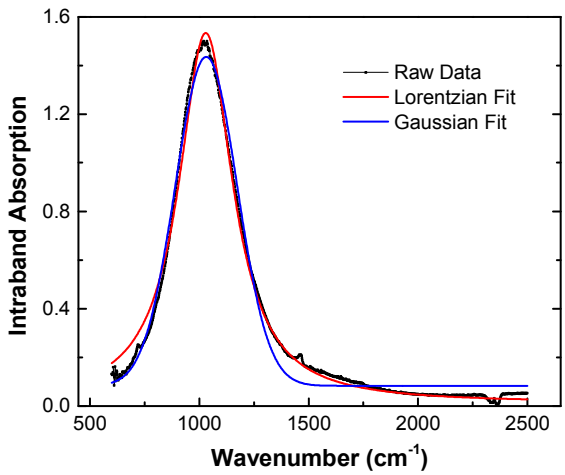

Figure S12. Intraband absorption of 14.5 nm HgS fitted with Lorentzian and Gaussian functions

Figure S12 shows that the line shape of 14.5 nm HgS is much closer to a Lorentzian function than to a Gaussian, which is typical of a homogeneous plasmon resonance.

12. Local field effect shift for the $1S_e-1P_e$ transition in QD^{2-}

The shift of the $1S_e-1P_e$ intraband energy due to the local field effect described in the main text was calculated in the $k \cdot p$ approximation, using the effective mass at $k = \pi/R$ for the estimation of the surface plasmon resonance. The results are shown in Figure S13. It shows that the blue shift is noticeable but less than 10% of the $1S_e-1P_e$ energy. Therefore, the intraband transition in the small doping level is well described without the local field correction.

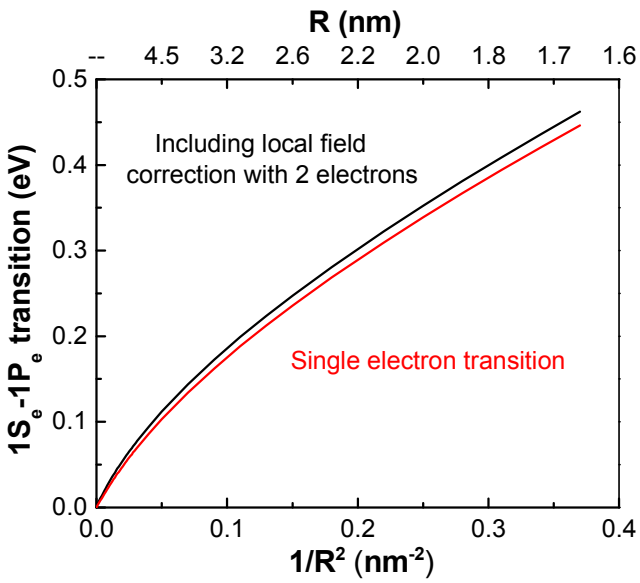

Figure S13. Red line: $k \cdot p$ prediction of the tuning of the $1S_e - 1P_e$ transition as a function of $1/R^2$, using $E_P = 4$ eV and $E_G = 0.65$ eV. Black line: After correction according to Eq. (4) in the main text to include the local field from the two transitions in a QD^{2-} dot.

13. CdS nanorods synthesis

The cadmium precursor was prepared by dissolving 0.05 of mmol cadmium(II) chloride in 8 mL of OAm, 10 mL of TCE, 0.8 g of diphenylamine and 0.2 mL of TOP at 80 ℃. The sulfide precursor was $(NH_4)_2S$. In a typical synthesis, 20 μL of $(NH_4)_2S$ was injected into 2 mL of cadmium precursor and reacted for 3 hours under vigorous stirring. The reaction was done at room temperature and in air. The final solution gave a yellow color. The nanorods were separated from the solution by the addition of methanol and centrifugation and then re-dispersed in TCE for further characterization.

Figure S14 shows a typical TEM image and XRD spectrum of CdS nanorods.

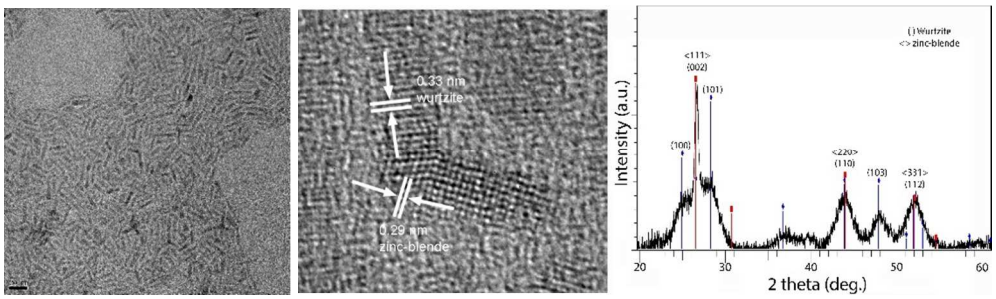

Figure S14. (From left to right) TEM, HRTEM and XRD of CdS nanorods. The red line in XRD spectrum indicates the bulk β-CdS (zinc-blende) peak positions, the blue line indicates the α-CdS (wurtzite)

The synthesized CdS are mostly nanorods with a small proportion of bipods, tripods and tetrapods. The short edge of a nanorod has an average length of 3.6 nm and the long edge varies between 10 nm to 20 nm. The XRD shows the CdS has a mixed phase of α-CdS and β-CdS. The existence of α-CdS is verified by the characteristic XRD peak at 2θ value around 37°. The existence of the β-CdS structure is inferred from the sharp peak around 26.5° as well as the relative intensity among the three peaks between 2θ value 40° to 55°. This mixed phase could also be observed directly from the HRTEM image of a bipod. The core of the bipod has the form of β-CdS with lattice fringe spacing of 0.29 nm (corresponds to β-CdS {200 planes), and its long arms are α-CdS with fringe spacing 0.33 nm (corresponds to α-CdS (002) planes). This indicates the nucleation of zinc-blende cores at room temperatures (kinetic control) followed by wurtzite arm growth on the core's four faces.[1-2] As a result, CdS nanorods, bipods, tripods and tetrapods are observed at the same time.

14. Interband quantum yield of HgS/CdS core/shell

The interband quantum yield (Φ) was measured using IR-26 dye dissolved in 1,2-dichloroethane as a reference. It was reported to have a quantum yield around 0.05%−0.1%.[3-4] Measure the PL and absorption of both the IR-26 solution and HgS/CdS solution (dissolved in TCE) gives the results in Figure S15a to S15c.

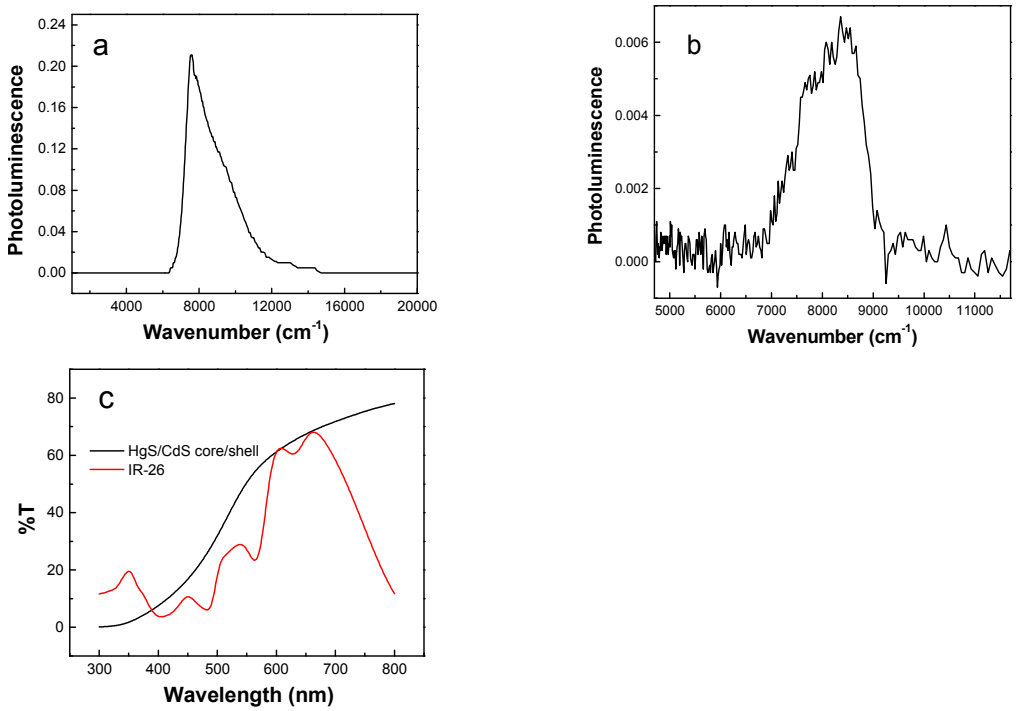

Figure S15. (a) PL of HgS/CdS core/shell; (b) PL of IR-26; (c) Transmittance of HgS/CdS and IR-26 solutions

The area beneath the PL curve is then integrated. Also the absorption of both solutions at 527 nm (the green laser used for PL measurement) is used to normalize the result. The quantum yield is then given by:

$$\Phi = \frac{\text{PL area of core/shell}}{\text{Absorption of core/shell (527 nm)}} \div \frac{\text{PL area of IR-26}}{\text{Absorption of IR-26 (527 nm)}} \times 0.1\%$$

The calculated quantum yield is ~5% using 0.1% for IR-26.

15. Reference

(1) Chen, M.; Xie, Y.; Lu, J.; Xiong, Y.; Zhang, S.; Qian, Y.; Liu, X. Synthesis of Rod-, Twinrod-, and Tetrapod-Shaped CdS Nanocrystals Using a Highly Oriented Solvothermal Recrystallization Technique. *Journal of Materials Chemistry* **2002**, *12*, 748-753.
(2) Yong, K.-T.; Sahoo, Y.; Swihart, M. T.; Prasad, P. N. Shape Control of CdS Nanocrystals in One-Pot Synthesis. *The Journal of Physical Chemistry C* **2007**, *111*, 2447-2458.

(3) Hatami, S., et al. Absolute Photoluminescence Quantum Yields of IR26 and IR-Emissive $Cd_{1-X}Hg_xTe$ and PbS Quantum Dots - Method- and Material-Inherent Challenges. *Nanoscale* **2015**, *7*, 133-143.
(4) Semonin, O. E.; Johnson, J. C.; Luther, J. M.; Midgett, A. G.; Nozik, A. J.; Beard, M. C. Absolute Photoluminescence Quantum Yields of Ir-26 Dye, PbS, and PbSe Quantum Dots. *The Journal of Physical Chemistry Letters* **2010**, *1*, 2445-2450.